Supplementary information

A rooted interphase on sodium via in-situ pre-implanting atom fluorine for high-performance sodium metal batteries

Chutao Wang,‡[a] Zongqiang Sun,‡[a], Lin Liu,[a] Hongbin Ni,[a] Qing Hou,[a] Jingmin Fan,[a] Ruming Yuan,[a] Mingsen Zheng,*[a,b] and Quanfeng Dong*[a,b]

[a.] *Department of Chemistry, College of Chemistry and Chemical Engineering, Collaborative Innovation Centre of Chemistry for Energy Materials, State Key Laboratory of Physical Chemistry of Solid Surfaces, Xiamen University, Xiamen, Fujian 361005, China. E-mail: qfdong@xmu.edu.cn; mszheng@xmu.edu.cn*

[b.] *Innovation Laboratory for Sciences and Technologies of Energy Materials of Fujian Province (IKKEM), Xiamen 361005, China.*

†Electronic Supplementary Information (ESI) available. See DOI:

‡These authors contributed equally to this work.

Experimental Section

Chemicals and Materials

Sodium metal was obtained from Sigma-Aldrich Corporation. The salts, solvents, including sodium hexafluorophosphate ($NaPF_6$), Propylene carbonate (PC), Fluoroethylene carbonate (FEC), diethyl carbonate (DEC), ethylene carbonate (EC), Ethyl Methyl Carbonate (EMC) were purchased from Duoduo Chemical Reagent Co., Ltd. with battery-grade purity. The Bistrifluoroacetamide (ECDA) was purchased from MACKLIN Co., Ltd., China. with purity of > 98%. Before preparing the electrolyte, the solvent was dried by 4Å zeolite to ensure that the water content was below 10 ppm. Prussian Blue cathodes were purchased from Naba Co., Ltd. Chemical reagents. Electrolytes were prepared by mixing the required amount of salt, solvent, additive. The usage of electrolyte in button cell was 90 μL. The preparation of electrolytes was all carried out in a glove box with O_2, and H_2O content < 1 ppm.

Characterization

The ionic conductivities (σ) and Electrochemical impedance spectroscopy (EIS) of different electrolytes at 25 °C were tested by electrochemical impedance spectroscopy (IM6, Zahner Elektrik, Germany) tests of button cells in a frequency range from 0.1 Hz to 10^5 Hz with an amplitude voltage of 5 mV. The electrodes were assembled with two stainless steels (SS||SS). The ionic conductivity (σ_{Na}) was calculated using the following equation:

$$\sigma_{Na} = \frac{L}{R \times S}$$

Where R is the bulk resistance, L is the thickness of the membrane, S is the contact area of inert electrode (stainless steel). In this work, the thickness of membrane is 0.2 mm, and the diameter is 15.6 mm.

X-ray powder diffraction (XRD) experiments were performed on a Rigaku Ultima IV X-ray diffractometer with a Cu Kα radiation (λ = 1.5418 Å) at a scan angle window between 20 and 80°. The morphological of cycles studies were obtained by HITACHI S-4800 field emission scanning electron microscopy (FESEM). To analyze the chemical composition of the solid electrolyte interphase (SEI) and cathode electrolyte interphase (CEI), characterization of electrodes after cycling using XPS measurements (Thermo Scientific ESCALAB Xi+,American). It is accompanied with depth profiling, which is performed by Ar^+ sputtering. High resolution transmission electron microscope (HRTEM) images were obtained from a TECNAI F30 at 300 kV. The cycled cells were disassembled in the glove box filled with argon (the contents of O_2 and H_2O were kept below 0.1 ppm) and the electrodes were washed with dimethyl ether (DME) before morphology and composition characterizations. The in-situ dynamic Na deposition behaviors were observed at 0.5 mA cm^{-2} for 30 min by ZOOM-0850C (SHANGHAI PUQIAN OPTICAL INSTRUMENT CO., LTD.) using Na as working electrode. The in-situ test used for the observations could be found in our previous work. Fourier transform infrared spectroscopy (FTIR) experiments were conducted by using a Nicolet iS50 FTIR spectrophotometer. ^{1}H-NMR tests were carried out (Bruker, Avance III HD 850MHz).

Electrochemical Measurements

The Na metal anodes were obtained by squeezing the Na metal foil (~1 mm) into many disks (Φ 14.0, ≥99.9%). Electrochemical cycling and rate tests were assembled by 2032-type coin batteries with glass fiber (Whatman GF-C) and tested by using a battery test system (Shenzhen NEWARE Co. LTD, China). The Na||Cu cells were using Cu foil as working electrode, Na metal disk as counter electrode. The coulombic efficiency (CE) of the Na||Cu cells was calculated by charge/discharge capacity, and the stripping cut-off potential was set to 1 V. Na||Na symmetric cells were assembled by using two piece of Na disks as working and counter electrodes. EIS in frequency ranges from 0.1 Hz to 10^5 Hz with amplitude of 5 mV. To perform the impedance test at different temperatures, the cells were first set aside for 2h at different temperatures. Cyclic voltammetry (CV, Squidstat prime) tests within potential range of -0.3-3 V vs. Na/Na$^+$ at scan rate of 1 mV s^{-1}. The oxidation potential of the electrolytes was tested by linear sweep voltammetry (LSV, Squidstat prime) of Na||SS cells. The chronoamperometry (CA) measurements was tested by Squidstat prime. The exchange current density of electrolytes was tested by Tafel plot (CHI660E, China) of Na||Na symmetric cells. The charge/discharge performance of electrolytes were obtained by assembled full cells using Prussian Blue (PB) as cathode, Na metal as anode and a piece of GF-C membrane as separator in an Ar-filled glove box (glove box with O_2 and H_2O content < 1 ppm). Cathode was prepared by coating a slurry composed of 80 wt% PB composite, 10 wt% Super P and 10 wt% polyvinylidene difluorides (PVDF) onto an Al foil substrate and dried under vacuum at 120 °C for 12 h. The low-loading of active materials was about 3 mg cm^{-2}. Cycle and rate tests were performed on the NEWARE battery test system at 25 °C. All Na||PB cells were tested in a voltage range between 2.4 - 4.5 V or 2.4 - 4.7 V vs. Na/Na$^+$. All full cells were activated for 2 cycles at 0.2 C. Low-temperature full cells test were performed by connect with NEWARE battery test system. The electrochemical performance and EIS at different temperatures was carried out within an RTP-80CT high and low temperature test chamber (Guangdong Huan Rui Test Equipment Co., Ltd, China). All cells were maintained at specified temperature for 2 h prior to testing. Final specific capacity was determined to the active mass of PB. The Na||PB full cells were fabricated with negative/positive capacity (N/P) ratio of 4 (the areal capacity of anode is 5.2 mAh cm^{-2} by pre-depositing Na on Cu foil and the areal capacity of cathode is 1.3 mAh cm^{-2}).

Computational Details

All calculations were carried out by using Perdew-Burke-Ernzerhof (PBE) gradient-corrected exchange-corrected functional with the projector augmented plane wave (PAW) method as implemented in the Vienna ab-initio simulation package (VASP). The plane wave kinetic energy cutoff was set to 400 eV. For ab initio molecular dynamics (AIMD) simulations, NVT ensemble was used at 300 K with a time step of 2 fs. A Nose thermostat with a Nose-mass parameter of 1.0 was employed to control the temperature oscillations during the simulations. Similar to the previous studies, a (5×5) five-layer slab of metallic Na with (110) exposing facet was used and a 15 Å vacuum spacing in the vertical direction was set. During AIMD simulations, the bottom three layers were fixed, while the upper two layers and the adsorbates thereon were allowed to be fully relaxed.

We calculated the mean squared displacement along the z-direction (MSD-z) relative to Na surface (the average positions of 25 Na atoms on the first layer) to determine whether the F atom has sunk into the Na subsurface and in xy plane (MSD-xy). That is,

$$\text{MSD-z} = [z_F(t) - z_{\text{Na}}(t)]^2$$

where $z_F(t)$ is the z position of F atom decomposed by FEC at time t, $z_{\text{Na}}(t)$ is the reference z position of the average of 25 Na atoms (labels 1 to 25) on the first layer at time t.

$$\text{MSD-xy} = [r_F(t) - r_F(0)]^2$$

where $r_F(t)$ is the xy position of F atom decomposed by FEC at time t, $r_F(0)$ is the reference xy position of F atom at time 0.
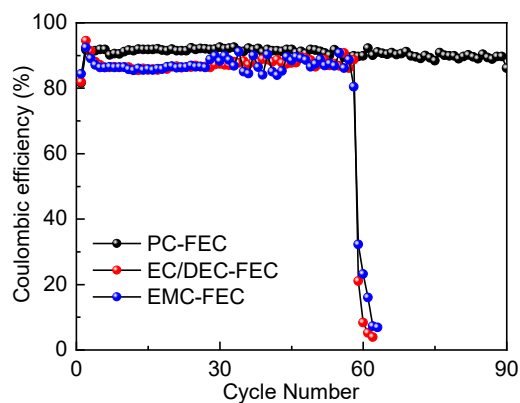
Fig. S1 Coulombic efficiency test in Na||Cu cells using electrolytes with different solvents at 1 mA cm^{-2} and 1 mAh cm^{-2}.

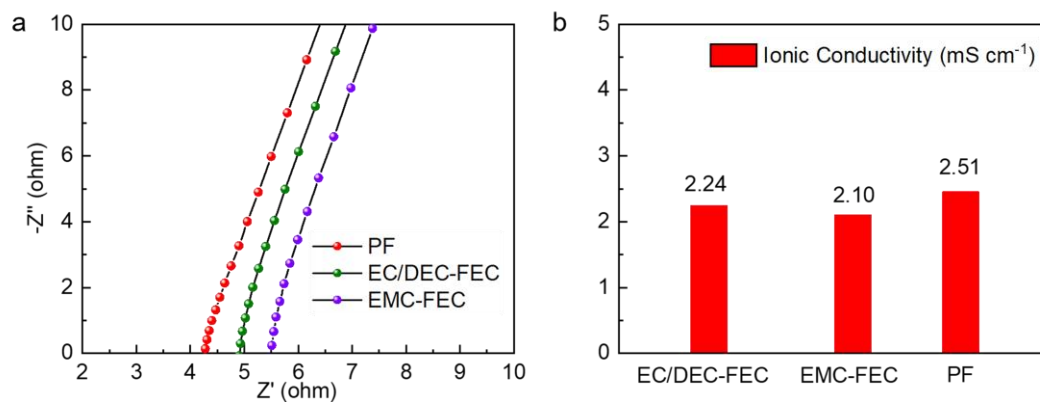
Fig. S2 (a) Ionic conductivity of the different electrolytes at room temperature. (b) Corresponding ionic conductivity calculation results.
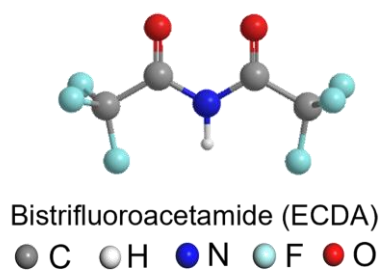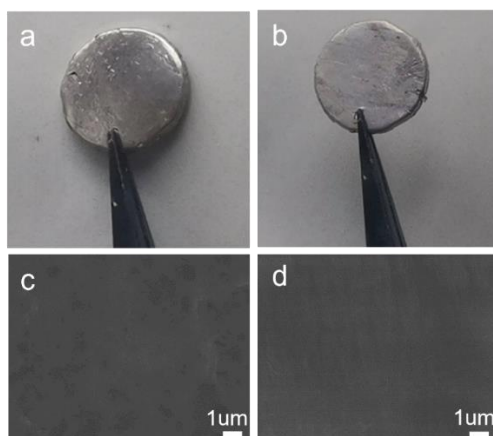

Bistrifluoroacetamide (ECDA)

● C ○ H ● N ○ F ● O

Fig. S3 The structural of ECDA.

Fig. S4 Digital images of (a) bare Na metal foils (b) Na metal foils after storing in PC solvent for 3 h. (c-d) Corresponding the Top-view SEM images.
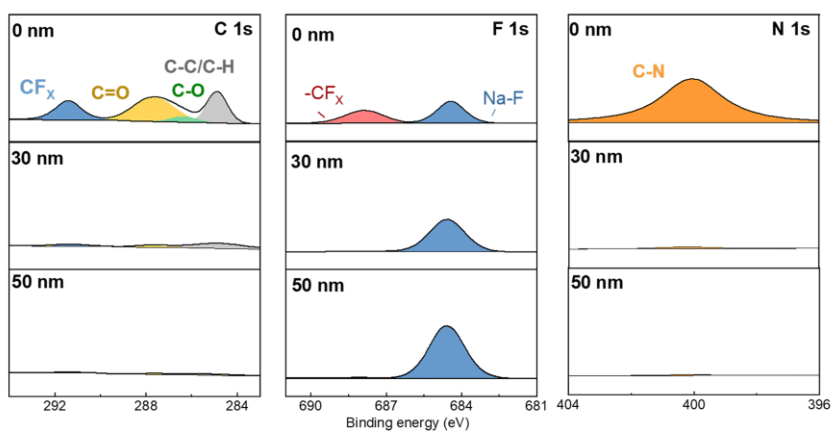
Fig. S5 C 1s, F 1s, N 1s XPS depth profiles of the Na metal anode in PC with 50 mM ECDA immersion.
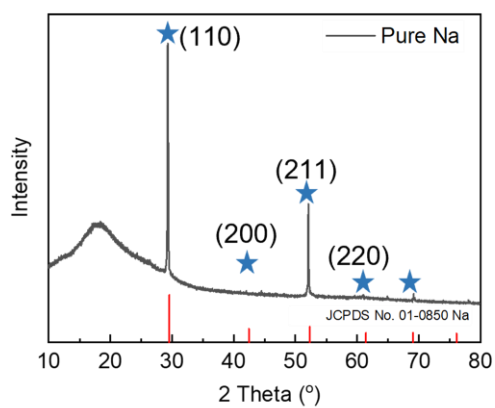
Fig. S6 XRD pattern of Pure Na

0 fs   200 fs   400 fs

800 fs   1600 fs   2500 fs
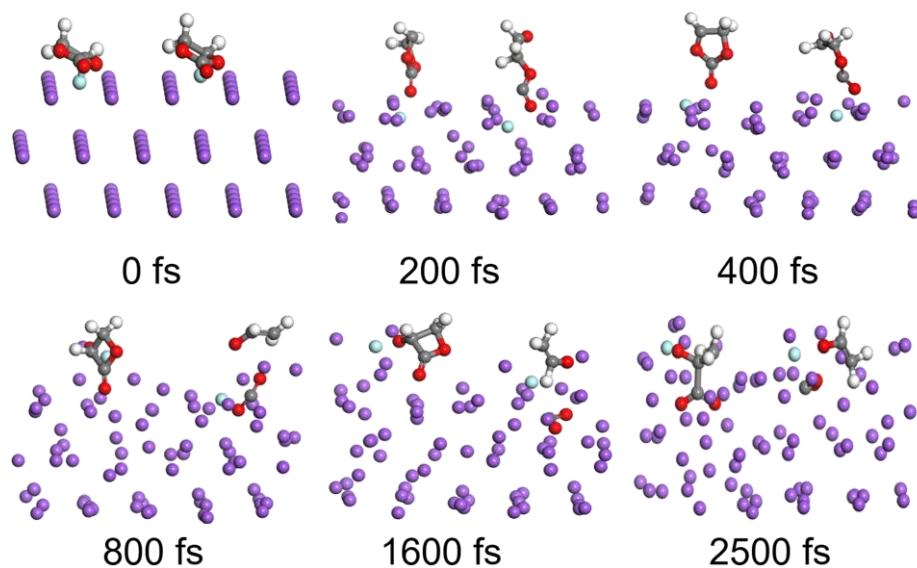
Fig. S7 Decomposition of two FEC molecules on Na (110) surface obtained from AIMD simulations.

0 fs   200 fs   400 fs

800 fs   1600 fs   2500 fs
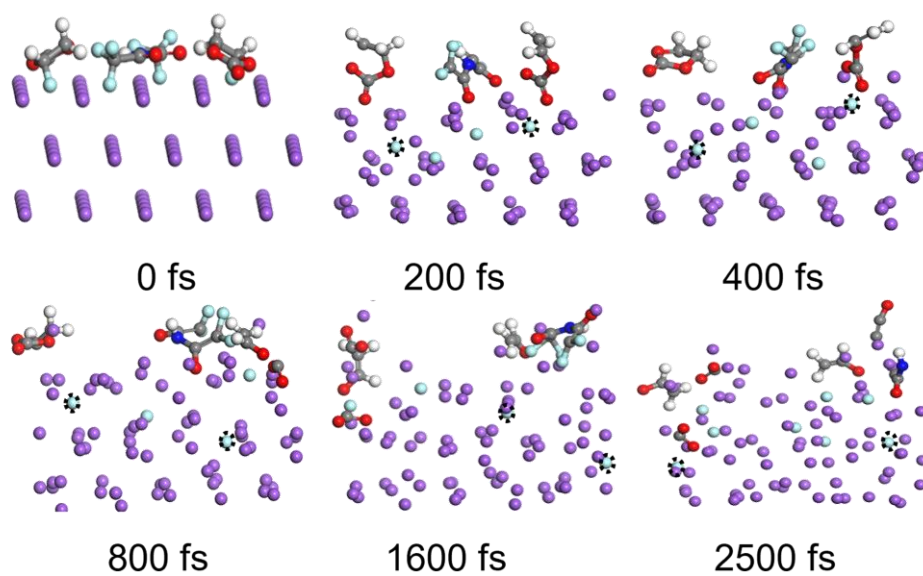
Fig. S8 Decomposition of two FEC molecules with a ECDA molecule on Na (110) surface obtained from AIMD simulations.
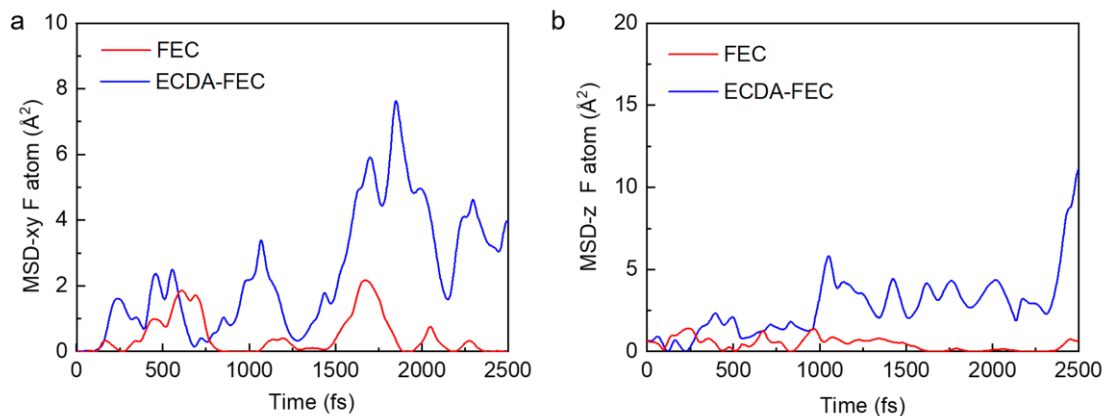
Fig. S9 MSD from FEC decomposition of F atoms in (a) the xy plane and (b) the z direction.
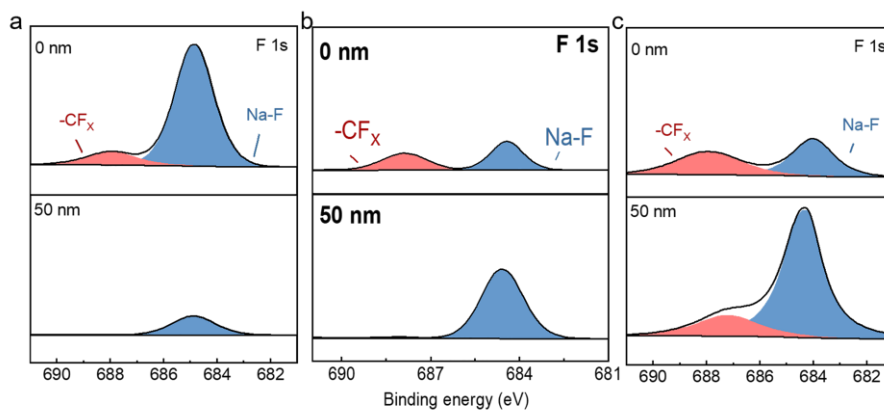
Fig. S10 F 1s XPS depth profiles of the Na metal anode in (a) FEC solution, (b) PC with 50 mM ECDA, (c) FEC with 50 mM ECDA immersion.
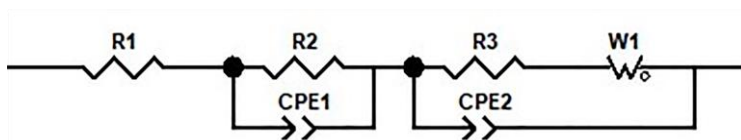
Fig. S11 The equivalent circuit models for EIS fitting of Na||Na cells, which the R_1 at high frequency is represent the resistance of electrolytes, and R_2, R_3 in the low frequency is represent the resistance of change transfer.
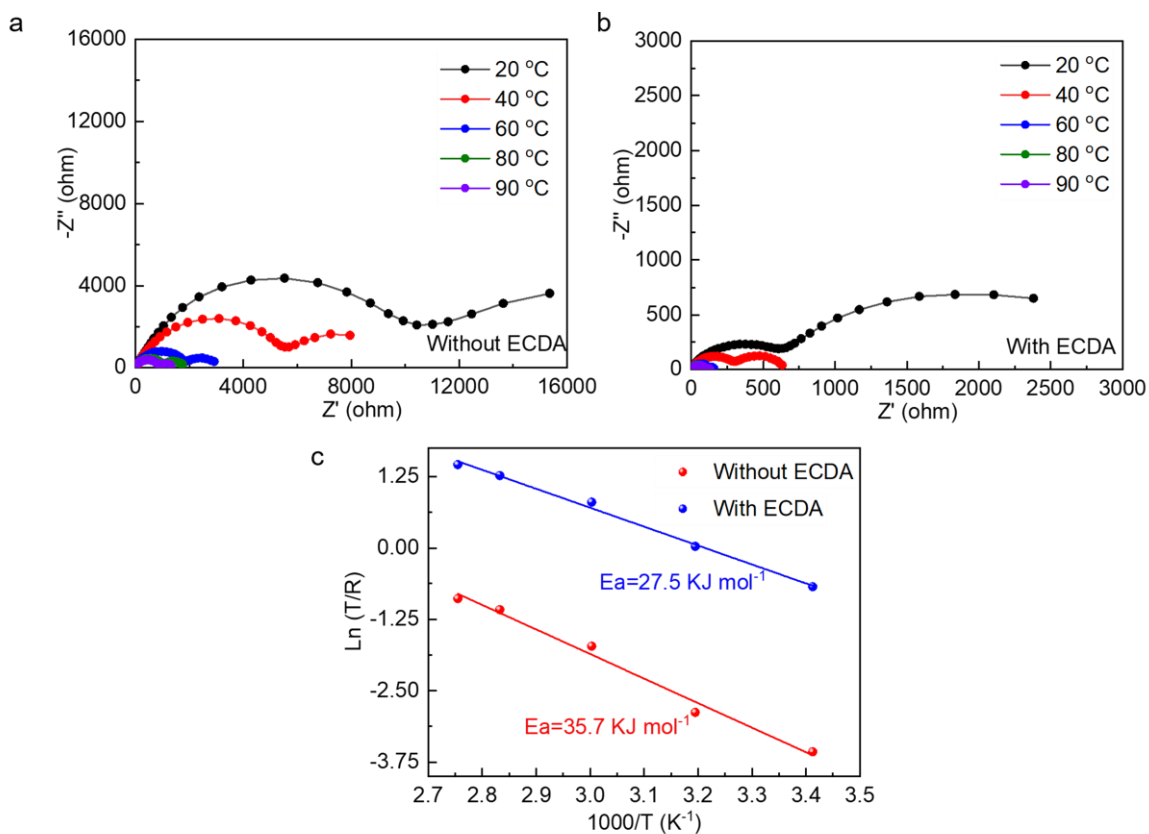
Fig. S12 (a-b) Impedance evolution with test temperatures for Na||Na cells in different electrolytes leave it for a day and no cycles. (c) Calculation of interface energy according to the Arrhenius formula.

Table S1 The fitting result of R_{int} at different temperature from 293 K to 363 K according to equivalent circuit of Na soak in the FEC solvent.

T (K)	R_{int} (Ω)	ln（T/R_{int}）	1000/T (K^{-1})
293	10459.1	-3.575	3.4130
313	5624.72	-2.889	3.1949
333	1890.33	-1.736	3.0030
353	1030.83	-1.071	2.8329
363	884.04	-0.890	2.7548

Table S2 The fitting result of R_{int} at different temperature from 293 K to 363 K according to equivalent circuit of Na soak in the FEC-ECDA solvent.

T (K)	R_{int} (Ω)	ln（T/R_{int}）	1000/T (K^{-1})
293	652.95	-0.801	3.4130
313	296.18	0.055	3.1949
333	123.27	0.994	3.0030
353	101.57	1.246	2.8329
363	90.49	1.389	2.7548
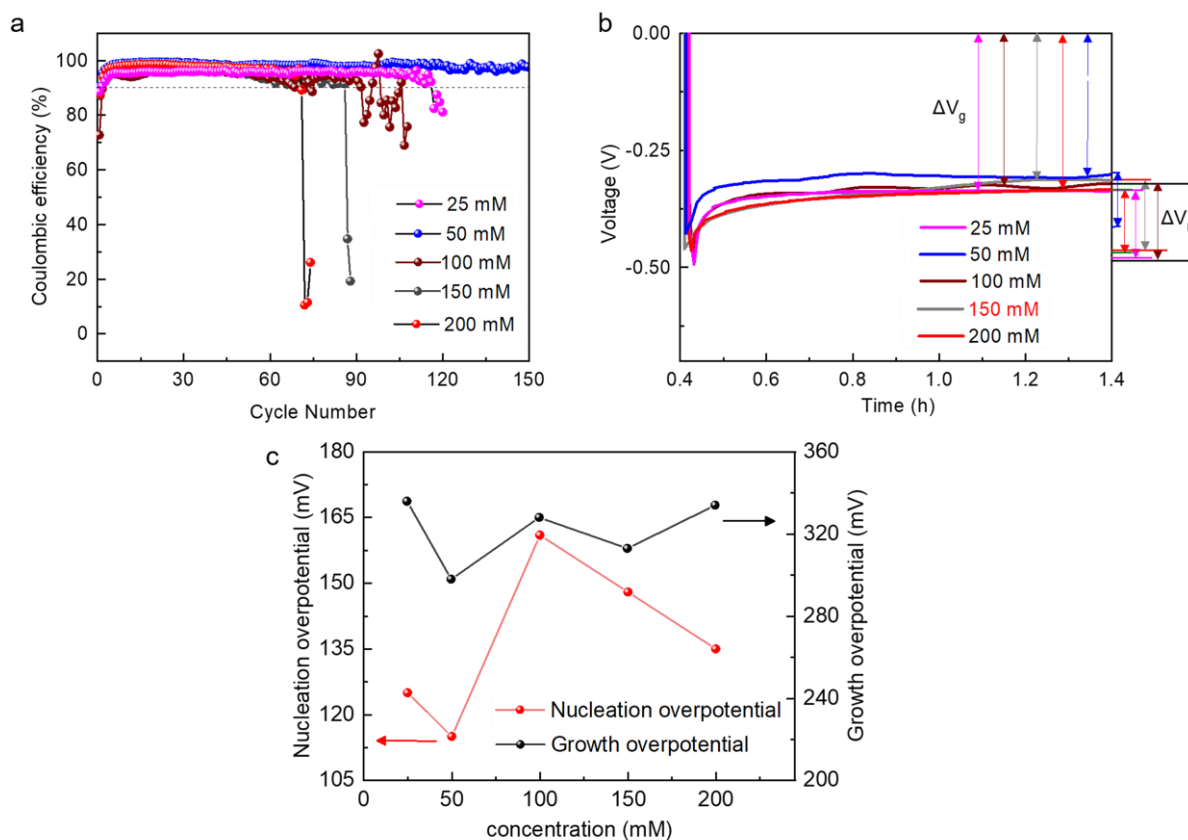
Fig. S13 Na||Cu cells in electrolytes with different additive concentrations at a current density of 1 mA cm^{-2} and a capacity of 1 mAh cm^{-2}. (a) Coulombic efficiency test (b) Corresponding the first voltage-cycle time profiles (c) Comparison of nucleation and growth overpotential.
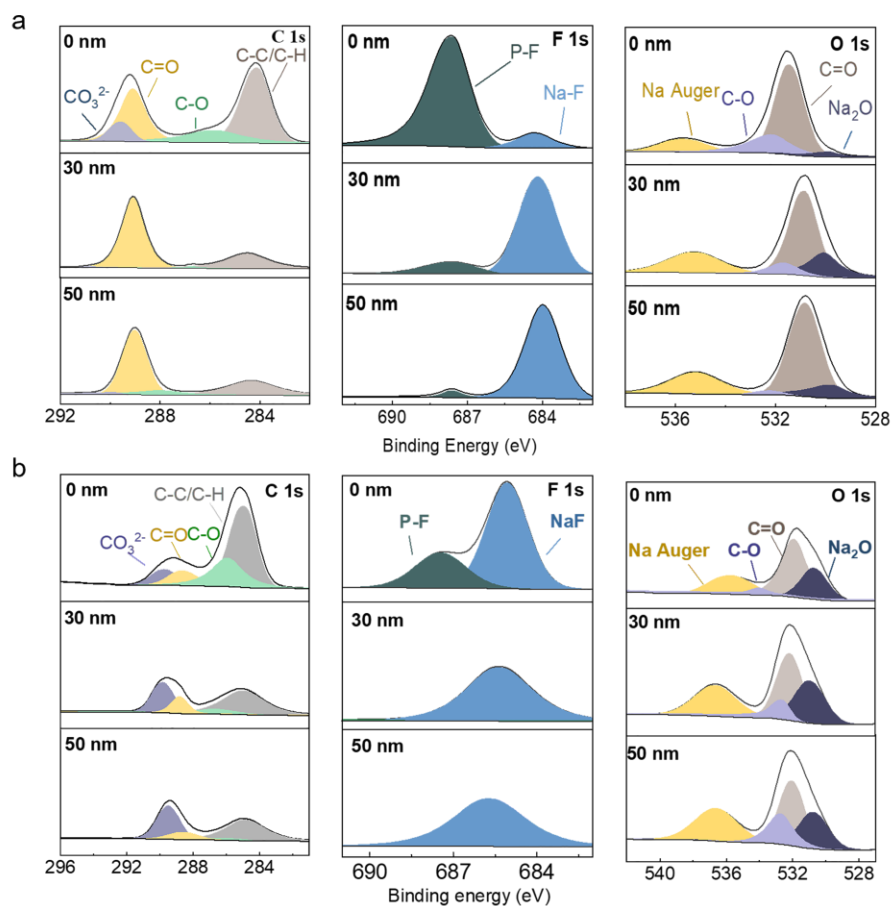
Fig. S14 C 1s, F 1s and O 1s XPS depth profiles of the Na metal anode after 15 cycles at a current density of 1 mA cm^{-2} and a capacity of 1 mAh cm^{-2} in (a) 1 M NaPF$_6$-PC and (b) PF-based electrolyte.

It can be seen 1 M NaPF$_6$ in PC electrolyte is easy to decompose and corrode electrode during cycles. From F 1s spectra, SEI form a small fraction of NaF because the decomposition of the NaPF$_6$. Meanwhile, the C 1s and O 1s spectra detected a large amount of C=O, indicting SEI contains many organic components.
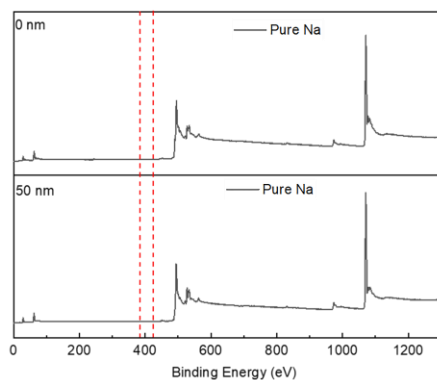
Fig.S15 XPS full spectrum of pure sodium metal.

To investigate thoroughly the NaN form due to residue N_2 in the glove box or XPS, we leave the sodium sheet in the glovebox filled with high purity argon (99.999%) for two days and then transfer it to the XPS unit for depth sputtering by high purity argon. There is no peak associated with Na_xN (397-398 eV) either at the surface or at depth, which also indicates that Na_xN did not originate from the glovebox or XPS test.

Based on the results of our experiments and theoretical calculations, we considered that ECDA undergoes the two-steps' reaction of chemical reduction reactionand electrochemical reduction reaction on the Na metal surface. The specific reaction processes are as follows:

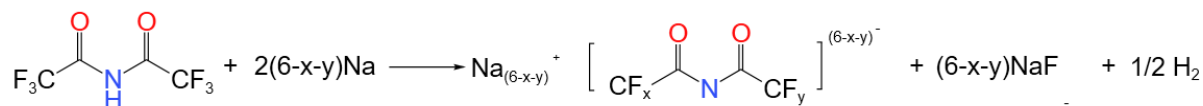Chemical reduction reaction step：

Fig. S16 (a) Possible chemical reduction reactions of ECDA on sodium metal.

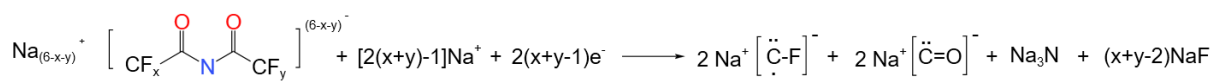Electrochemical reduction reaction step：

Fig. S16 (b) Possible electrochemical reduction reactions of ECDA on sodium metal.

During the chemical reduction reaction, the sodium metal as a strong reducing agent can lose electrons to form Na^+, making the reaction of ECDA on the sodium metal preferentially through the breaking of the C-F bond to produce NaF. Moreover, due to the presence of acidic hydrogen atoms (H) in the -NH- in (CF_3-CO-NH-CO-CF_3), indicates that -NH- is prone to fracture. Whereas the lone pair of electrons of the amino nitrogen will be conjugated to the π-electrons of the carbonyl group, the electron cloud on the nitrogen is less dense and therefore easier to accept.

During the electrochemical reaction, the resulting sodium salt (NaX) is further completely decomposed on the surface of the sodium metal electrode and the final decomposition products are small molecular compounds, which are unlikely to undergo further reactions.
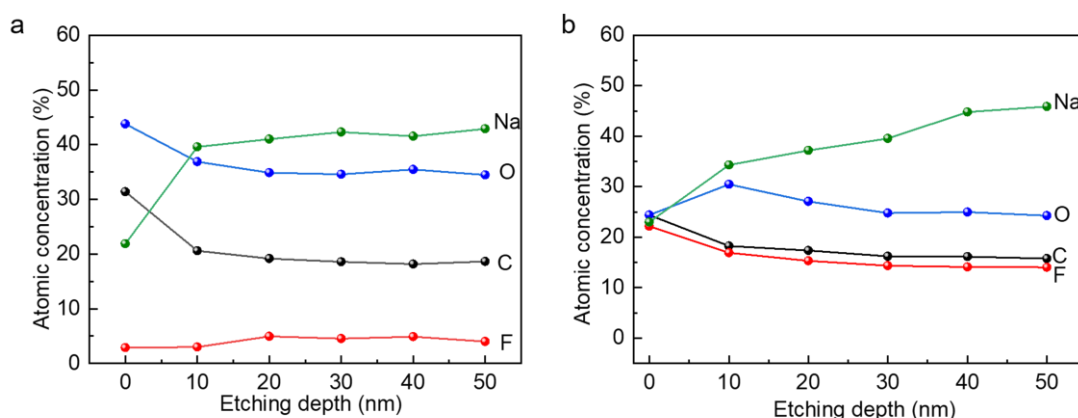

Fig. S17 Atomic ratios of the C 1s, O 1s, Na 1s and F 1s on the Na metal at various durations of Ar^+ sputtering in (a) PC-based electrolyte and (b) PF-based electrolyte.
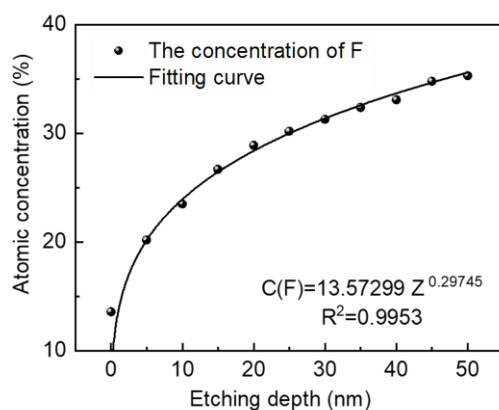
Fig. S18 The variation of eleven F concentrations with sputtering depth was fitted using an exponential function in the PFDA-based electrolyte.

First of all, the concentration gradient can be expressed as a function of:

$$\nabla C = (\partial C/\partial x, \partial C/\partial y, \partial C/\partial z)$$

$\partial C/\partial x$ denotes the partial derivative of the function C with respect to x, $\partial C/\partial y$ denotes the partial derivative of the function C with respect to y, and $\partial C/\partial z$ denotes the partial derivative of the function C with respect to z.[1]

Since our system only considers the change of z-direction by sputtering process, the function could be simplified to $\nabla C = (\partial C/\partial z)$. The F concentration and sputtering depth follow the exponential function $y = aX^b$. The function after passing the partial derivative is still an exponential function, i.e., it is still a function of the concentration variation. Therefore, we consider that an F concentration gradient is formed at the z-direction (Perpendicular to the Na metal electrode/electrolyte interface).[2-6]
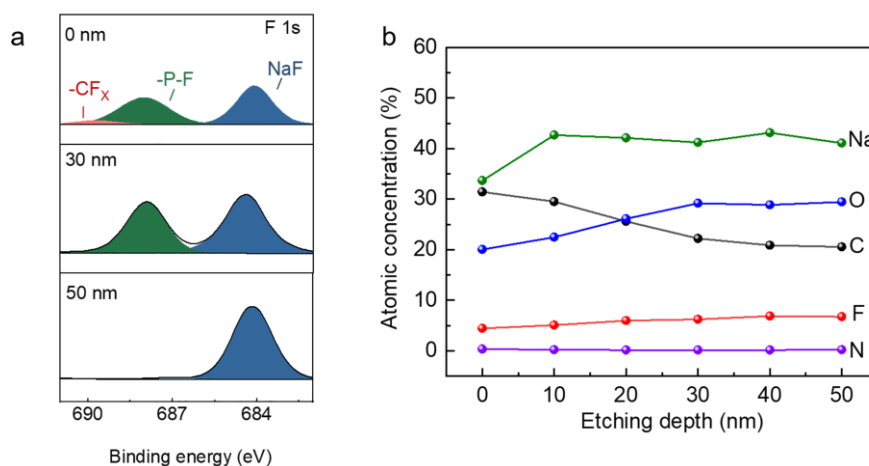

Fig. S19 (a) F 1s XPS depth profiles of the Na metal anode and (b) Atomic ratios of the C 1s, O 1s, Na 1s and F 1s on the Na metal at various durations of Ar+ sputtering after 15 cycles in 1 M $NaPF_6$ in PC with 50 mM ECDA electrolyte.

For the sodium metal using ECDA alone, both 0 nm and 50 nm depths still have a high amount of organic carbon, as well as ~7% (50 nm) F content, Which suggests that although ECDA can also participate in the formation of SEI by breaking the C-F bond, the dominated components of SEI is still organic compounds probably derived from the decomposition of other components in the electrolyte (e.g., PC).
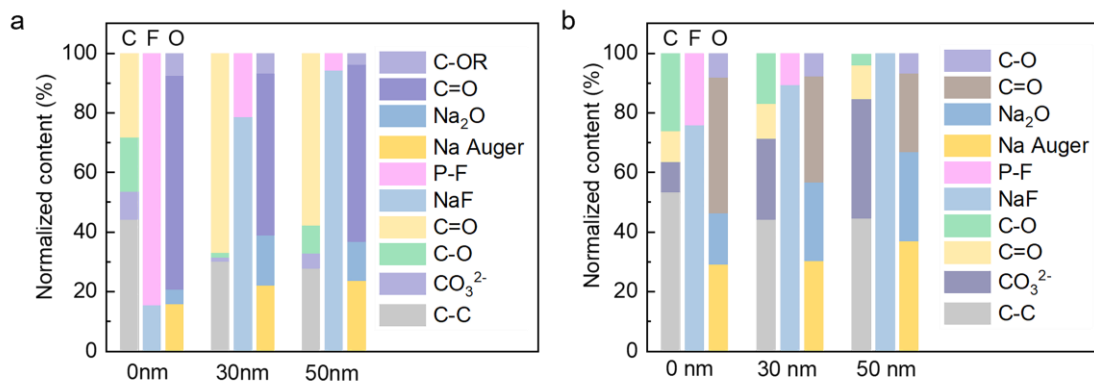
Fig. S20 Normalized ratios of different species in the SEI formed in (a) PC-based electrolyte and (b) PF-based electrolyte.

E_{ads}= -0.71 eV
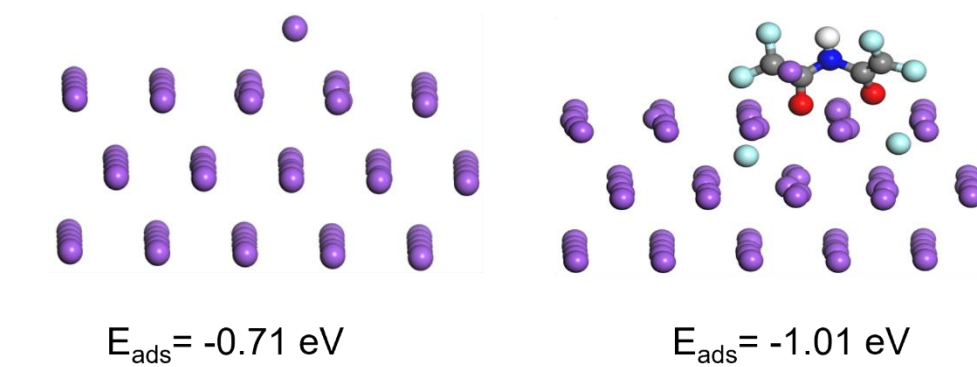
E_{ads}= -1.01 eV

Fig. S21 Simulation of foreign Na adsorption (deposition) from DFT with and without ECDA action on the Na (110) surface.
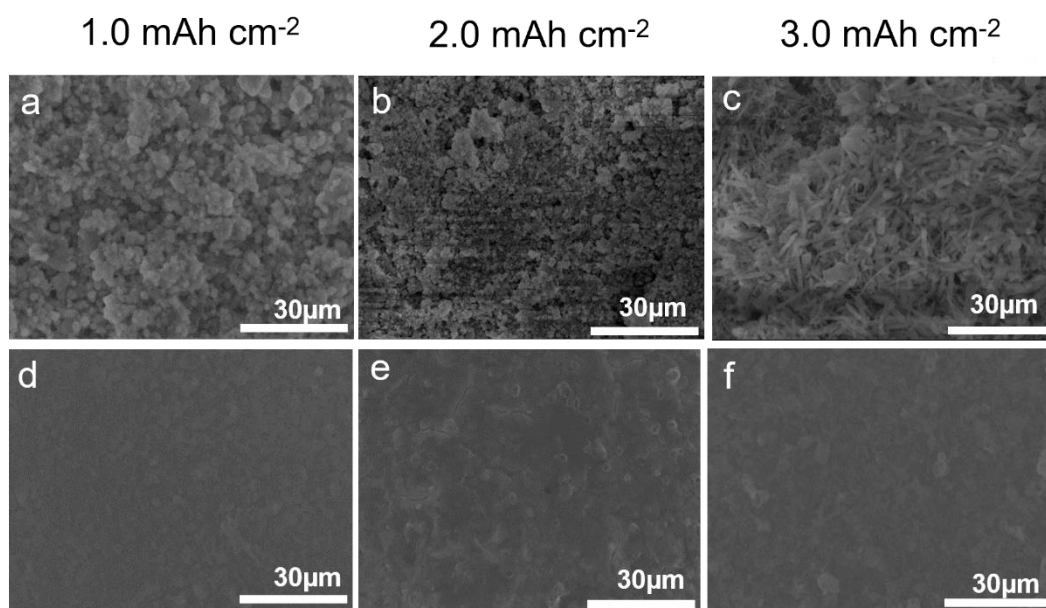
Fig. S22 Top SEM image of Cu foil cycled in Na||Cu cells after 10 cycles using (a-c) PF-based electrolyte, (d-f) PFDA-based electrolyte at 1.0 mA cm^{-2} and different capacity of 1.0, 2.0, 3.0 mAh cm^{-2}.

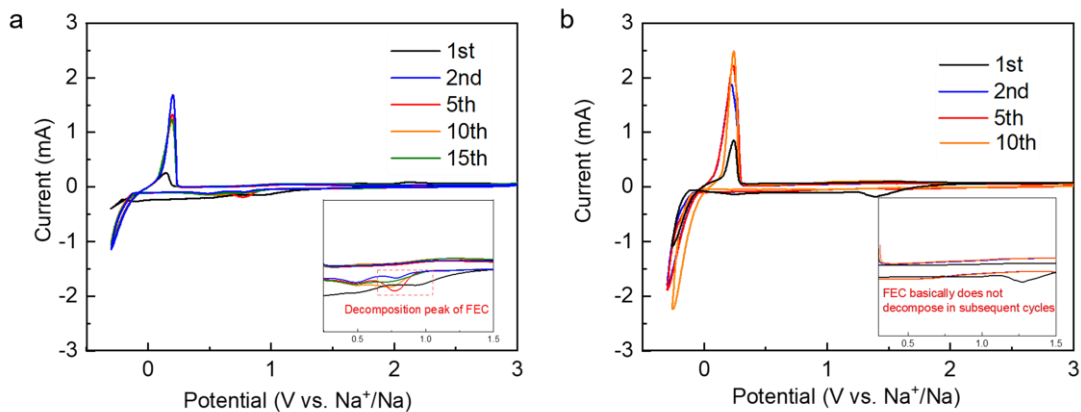Fig. S23 Schematic diagram of electrolytic cell (Na||Na) device for in situ optical microscopy.

Fig. S24 Cycle voltammetry (CV) curves of Na||Cu cells at a scan rate of 1 mV s^{-1} (a) PF-based electrolyte, (b) PFDA-based electrolyte.

Ion transport will usually appear as a symmetrical and reversible redox peak, with the peak current density corresponding to the rate of ion transport. If the redox peaks are symmetrical, the peak currents vary with the cycling process, which indicates the involvement of ion transport. For both PF and PFDA-based electrolytes, there is a more symmetrical and reversible plating/stripping redox peak, with Na$^+$ being transported at the SEI and undergoing stable plating/stripping on the Na metal.[7-12]
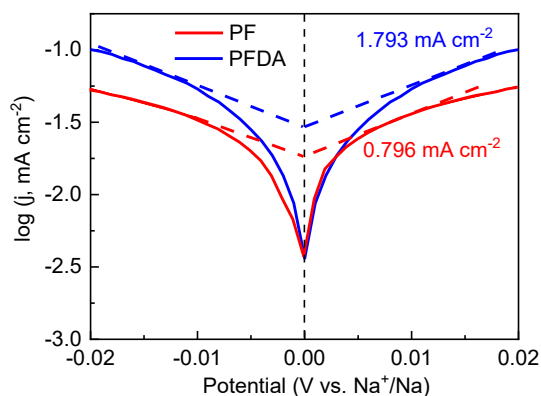

Fig. S25 Tafel plots of the corresponding Na||Na cells for analysis of the exchange current density in the PF-based and PFDA-based electrolytes.

Tafel experiments to illustrate Na$^+$ transport in the SEI. the larger exchange current density values in the PFDA-based electrolyte may indicate that the SEI layer has a low resistance that favors rapid Na$^+$ transport. [7-12]
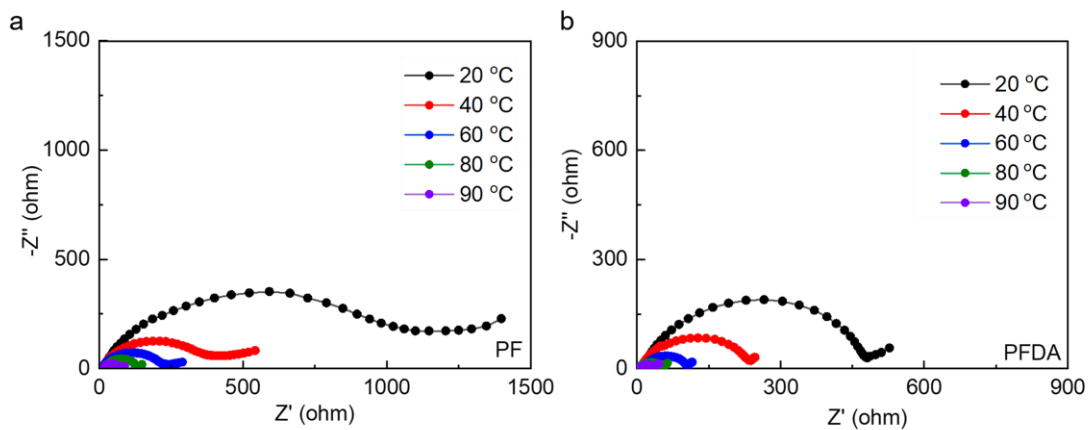
Fig. S26 Impedance evolution with test temperatures for Na||Na cells in (a) PF-based electrolyte, (b) PFDA-based electrolyte after 10 cycles.

Table S3 The fitting result of R_{int} at different temperature from 293 K to 363 K according to equivalent circuit in the PF-based electrolyte.

T (K)	R_{int} (Ω)	ln（T/R_{int}）	1000/T (K^{-1})
293	1144.1	-1.3678	3.4130
313	409.72	-0.274	3.1949
333	240.33	0.337	3.0030
353	133.83	0.982	2.8329
363	71.04	1.643	2.7548

Table S4 The fitting result of R_{int} at different temperature from 293 K to 363 K according to equivalent circuit in the PFDA-based electrolyte.

T (K)	R_{int} (Ω)	ln（T/R_{int}）	1000/T (K^{-1})
293	481.06	-0.496	3.4130
313	232.06	-0.299	3.1949
333	104.27	1.160	3.0030
353	53.57	1.885	2.8329
363	39.49	2.218	2.7548
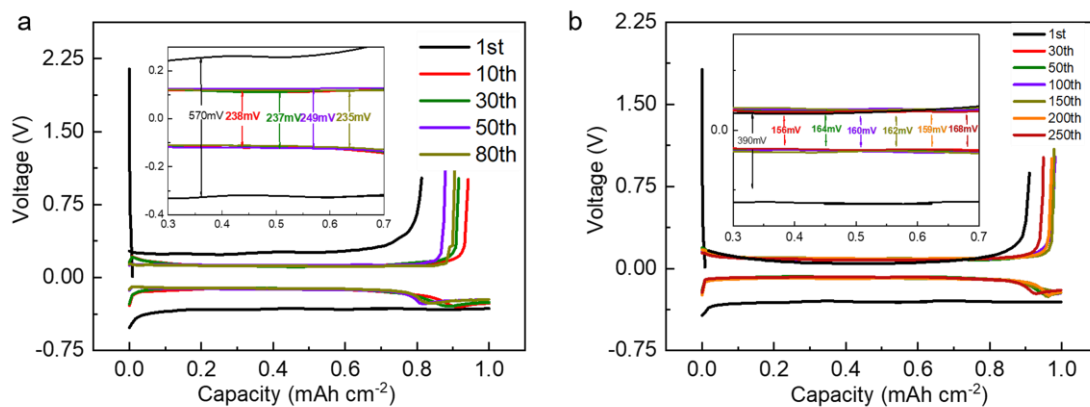
Fig. S27 Selective plating/stripping profiles for Na||Cu cells in (a) PF-based electrolyte (b) PFDA-based electrolyte at a current density of 1 mA cm^{-2} and a capacity of 1 mAh cm^{-2}. (The inset shows the difference in voltage hysteresis at different cycles)
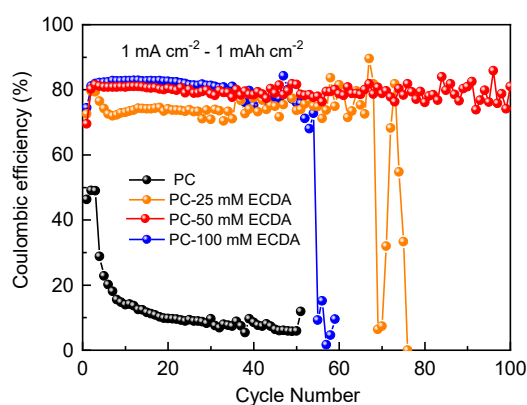

Fig. S28 Coulombic efficiency test in Na||Cu cells using PC electrolytes with different ECDA concentrations at a current density of 1 mA cm^{-2} and a deposition capacity of 1 mAh cm^{-2}.
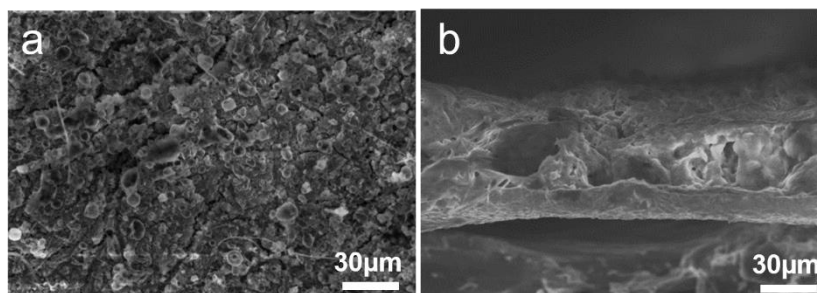
Fig. S29 (a-b) SEM image on copper foil of PC-50 mM ECDA electrolyte after 50 cycles.

The performance (coulomb efficiency and cycle life) of Na||Cu cells using ECDA alone is also quite ordinary and far from the higher requirement. More regrettably, the electrolyte using ECDA alone showed loose and porous surface and large particle deposition during sodium deposition process, which once again proved that ECDA itself does not possess the ability to construct excellent F-rich SEI in the sodium-metal cell system.
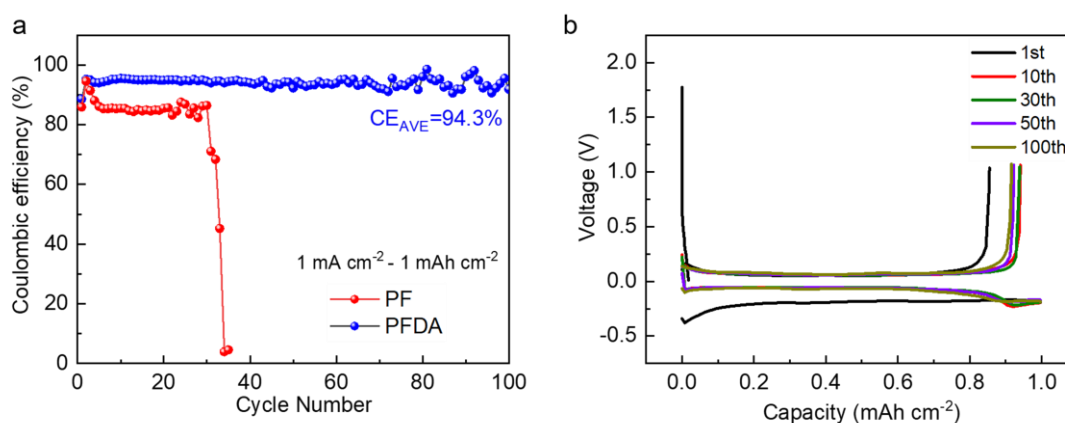

Fig. S30 Electrochemical performance of Na||Cu cells after 100 cycles following a failed cycle in a PF-based electrolyte (a) Coulombic efficiency test in PFDA-based electrolyte electrolytes at a current density of 1 mA cm^{-2} and a capacity of 1 mAh cm^{-2}. (b) Corresponding the selective plating/stripping profiles for Na||Cu cells.
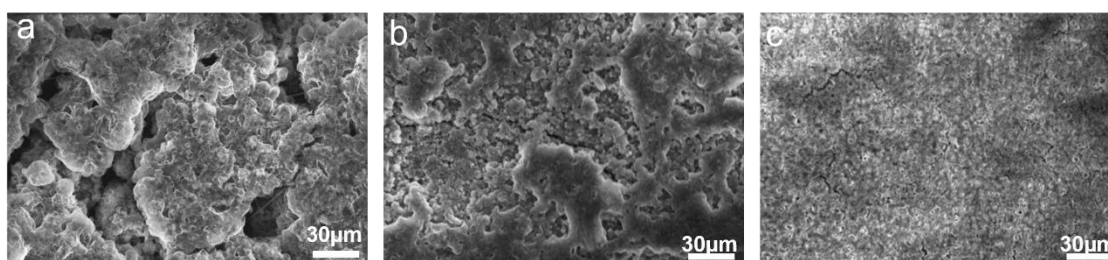

Fig. S31 (a) SEM image on copper foil after short circuiting of PF-based electrolyte cycle. (b) SEM image on the copper foil after 25 cycles by replacing to PF-based electrolyte without replacing the sodium sheet, copper foil and separator. (c) SEM image on the copper foil after 50 cycles by replacing to PFDA-based electrolyte without replacing the sodium sheet, copper foil and separator.
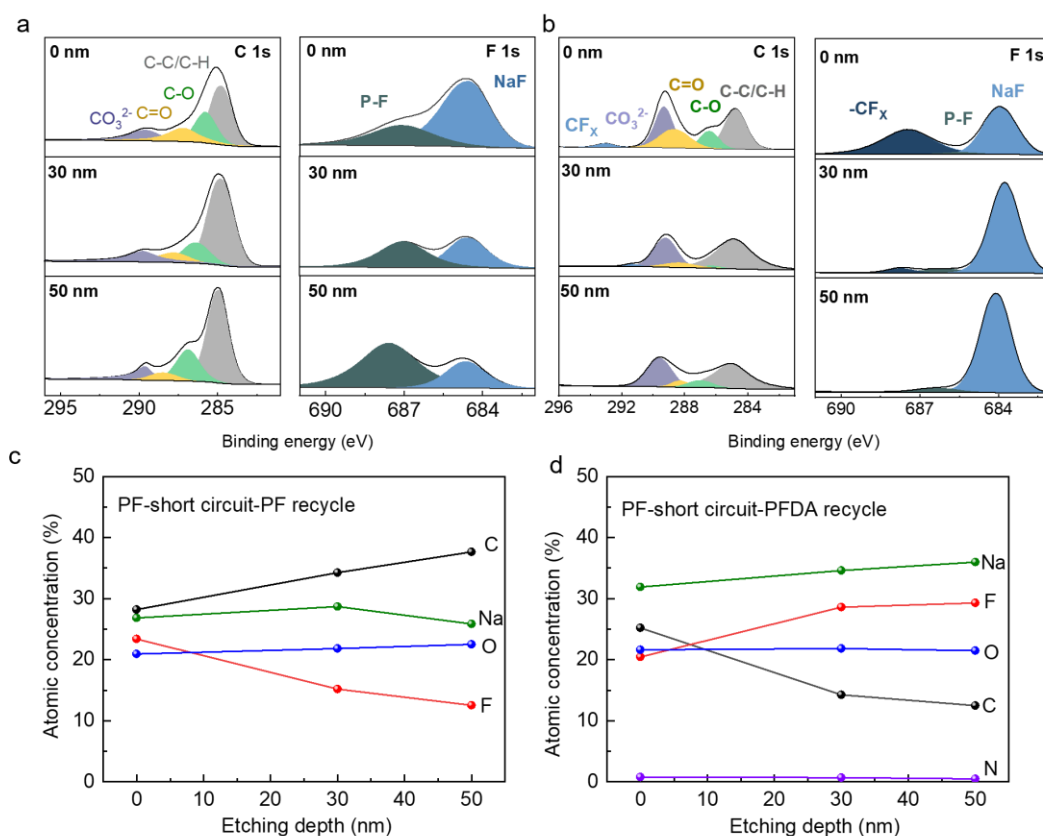
Fig. S32 (a-b) XPS depth curves of C 1s and F 1s spectra of Na metal anode after re-circulating 30 cycles by adding PF-based electrolyte and PFDA-based electrolyte without replacing sodium sheet, copper foil and septum in short-circuit cell. (c-d) Corresponding atomic concentrations of C 1s, O 1s, N 1s, F 1s and Na 1s spectra on Na electrodes in different systems with different depths of Ar⁺ sputtering.

First, from the CE of the Na||Cu cell in Fig. S30, the PF-based electrolyte was able to reactivate the shorted cell, but it quickly failed again after 30 cycles. From the SEM image in Fig. S31, the Na||Cu cell shows a very great deposited particle morphology after short-circuiting of the PF-based electrolyte, and even many moss-like dendrites have appeared. The addition of PF-based electrolyte also did not restore the broken deposited morphology. Surprisingly, we were able to re-cycle the cell by adding only the PFDA-based electrolyte, and the cycling process was able to cover the original porous mossy morphology that had been destroyed (Fig. S31c). The originally formed fragile SEI was gradually replaced by R-SEI throughout the cycling process, and stable Na plating/stripping was restored. Although this makes the SEI thicker, it is excellent enough compared to the worse and thicker SEI accumulated by PF-based electrolyte.

Furthermore, we used XPS to analyze the structure and composition of SEI after 30 cycles of two electrolyte recirculation to illustrate the advantages of R-SEI (Fig. S32). After recirculation of the PF-based electrolyte, the amount of organic carbon in the re-formed SEI is increasing, and there is still a large amount of P-F within the SEI, with less inorganic species such as NaF, etc. The SEI is still very unstable. In combination with the SEM results it was also found that this SEI deposited Na was still porous and not dense and basically did not improve the interface of the short circuit cell. In contrast, recirculation with PFDA-based electrolytes was able to form a good interface on the electrode surface again. The XPS results show a rapid decrease in the organic carbon content and an increasing content of elemental F after recirculation, i.e., an increasing content of inorganic NaF. In contrast, recirculation with PFDA-based electrolytes was able to form a good interface on the electrode surface again. The XPS results show a rapid decrease in the organic carbon content and an increasing content of elemental F after recirculation, i.e., an increasing content of inorganic NaF. This demonstrates that ECDA in PFDA-based electrolyte is functioning through decomposition to improve the structure and composition of SEI with excellent sodium ion transport and promote the formation of smaller deposited particles.
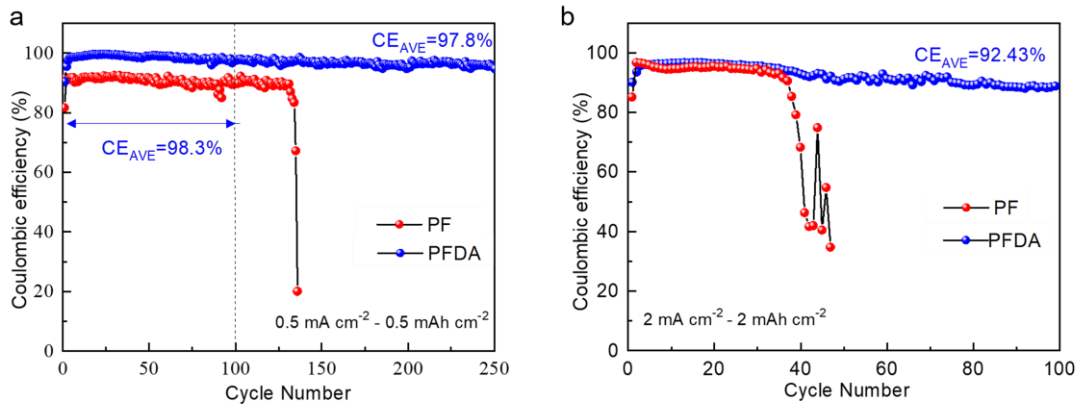
Fig. S33 Coulombic efficiency test in Na||Cu cells using different electrolytes at (a) a current density of 0.5 mA cm^{-2} and a capacity of 0.5 mAh cm^{-2} and (b) a current density of 2 mA cm^{-2} and a capacity of 2 mAh cm^{-2}.

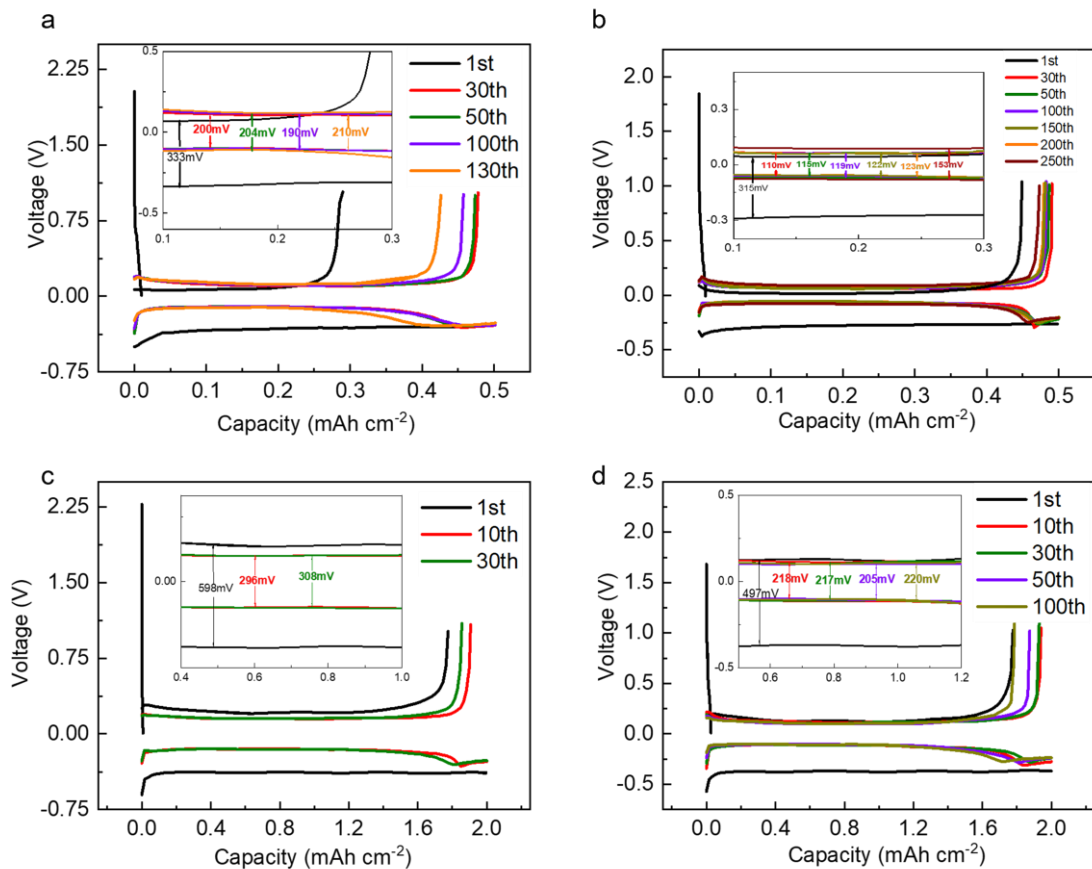

Fig. S34 Selective plating/stripping profiles for Na||Cu cells in (a-b) PF-based electrolyte and PFDA-based electrolyte at a current density of 0.5 mA cm^{-2} and a capacity of 0.5 mAh cm^{-2}. (c-d) PF-based electrolyte and PFDA-based electrolyte at a current density of 2 mA cm^{-2} and a capacity of 2 mAh cm^{-2}. (The inset shows the difference in voltage hysteresis at different cycles)
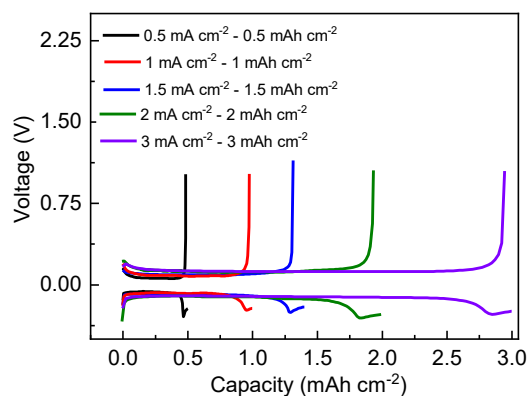
Fig. S35 Profiles of Na plating/stripping on a Cu foil substrate at different current densities of 0.5, 1.0, 2.0, 3.0 mA cm^{-2} and different capacity of 0.5, 1.0, 2.0, 3.0 mAh cm^{-2} in PFDA-based electrolyte.
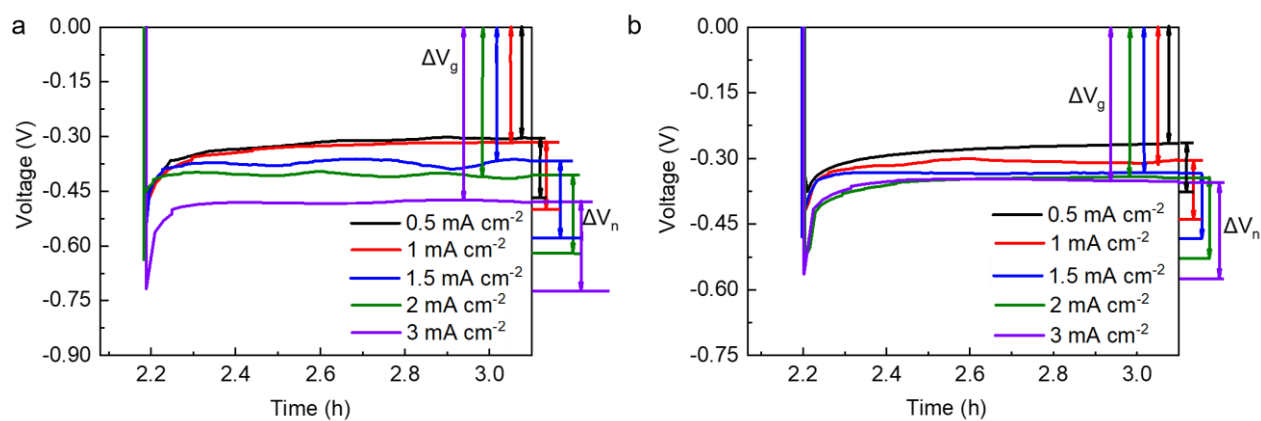

Fig. S36 Initial plating profiles at different current densities of 0.5, 1.0, 2.0, 3.0 mA cm^{-2} in (a) PF-based electrolyte, (b) PFDA-based electrolyte for comparing the Nucleation (ΔV_n) and growth (ΔV_g) overpotential.

Table S5 Performance comparison and summary of Na||Cu cells with different conditions and electrolytes in the reported research.

| Electrolyte	Current density (mA cm^{-2})	Capacity (mAh cm^{-2})	CE (%) (cycles)	Journal
PFDA-based electrolyte	0.5	0.5	**97.8 (250)**	**This work**
	1	1	**97.3 (250)**	
	2	2	**92.4 (100)**	
1.0 M NaClO$_4$ in EC/PC/10% SiO$_2$- IL-ClO$_4$	/	/	90.0 (100)	*Nat. Commun.* 2016, **7**, 11722.
1.0 M NaClO$_4$ in EC/PC /DAIM	1	1	93.0 (120)	*Adv. Mater.* 2017, **29**, 1605512.
1.0 M NaTFSI in TMP/FEC/HFE	0.5	0.5	90.0 (100)	*Adv. Funct. Mater.* 2021, **23**, 2103522.
1.0 M NaPF$_6$ in FEC/PC /PFMP	0.5	0.5	94.0 (100)	*Energy Environ. Sci.* 2020, **13**, 1788.
0.8 M NaPF$_6$ in FEC/EMC/HFE/SnF$_2$	1	2	95.3 (100)	*Energy Environ. Sci.* 2021, **14**, 4936.
NaCl-buffered AlCl$_3$/[EMIm]Cl/EtAlCl	0.5	0.25	95.0 (100)	*Nat. Commun.* 2019, **10**, 3302.
1.0 M NaPF$_6$ in TTE/FEC/DMTP	0.5	0.5	95.2 (100)	*Adv. Funct. Mater.* 2022, **26**, 2109378.
1.0 M NaPF$_6$ in EC/PC/ TMTD	/	/	94.3 (Aurbach)	*Nano Lett.* 2021, **21**, 619.
1.0 M NaTFSI in FEC/FEMC/FB (3:3:4 vol)	1	1	92.7 (100)	*Nano Energy* 2022, **103**, 107746.
1.0 M NaClO$_4$ in EC/PC (1/1 by volume) / 5 wt.% FEC	1	1	<90 (50)	*Chem. Commun.* 2018, **54**, 2381.
1.0 M NaTFSI in /SL/FEC/HTCN (7:2:1 vol)	1	2	90.1 (100)	*ACS Energy Lett.* 2022, **7**, 2032.
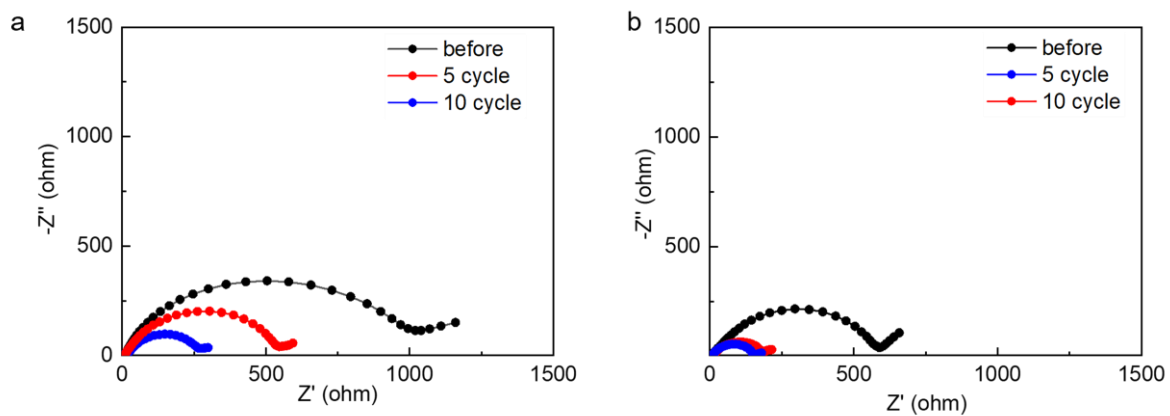
Fig. S37 Nyquist plots of Na||Na symmetric cells at different cycles in (a) PF-based electrolyte, (b) PFDA-based electrolyte. (The equivalent circuit models for EIS fitting show as Figure S7)
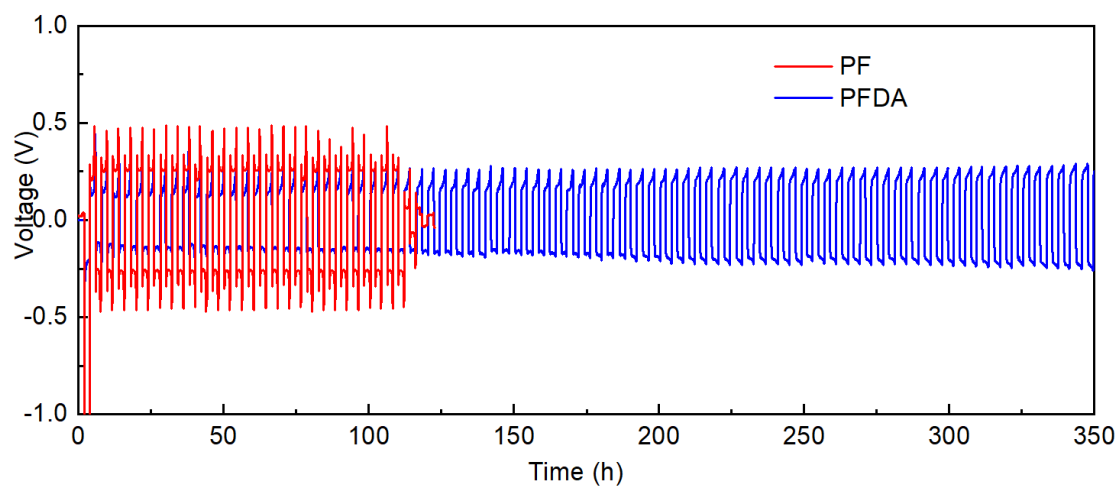

Fig. S38 Voltage profiles of Na||Na symmetric cells in PF-based electrolyte and PFDA-based electrolyte of 2 mA cm^{-2} and 4 mAh cm^{-2} Na capacity.
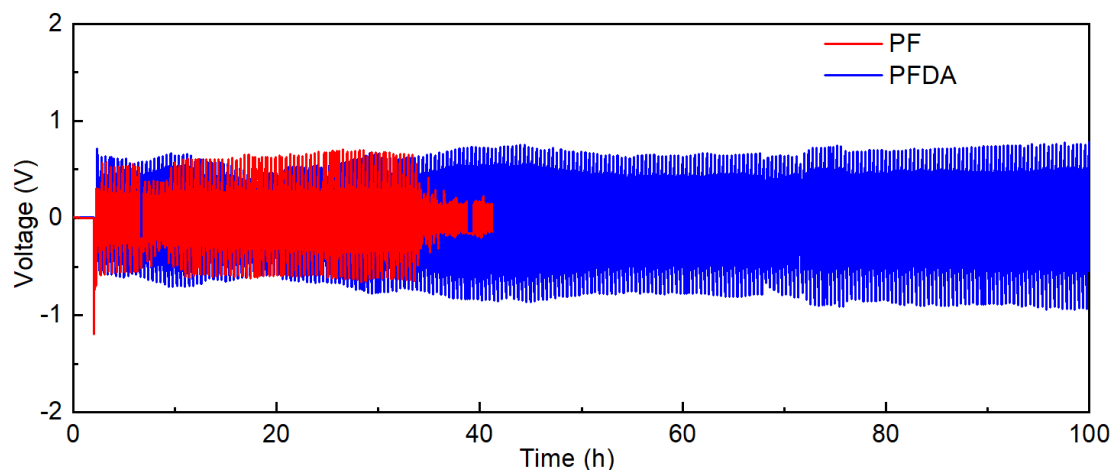
Fig. S39 Voltage profiles of Na||Na symmetric cells in PF-based electrolyte and PFDA-based electrolyte of 5 mA cm^{-2} and 1 mAh cm^{-2} Na capacity.
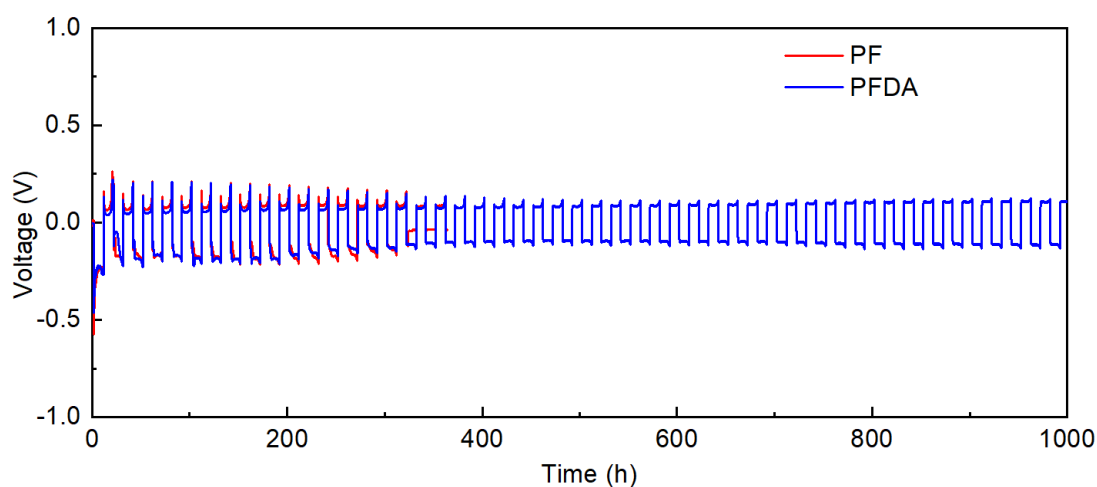

Fig. S40 Voltage profiles of Na||Na symmetric cells in PF-based electrolyte and PFDA-based electrolyte of 1 mA cm^{-2} and 10 mAh cm^{-2} Na capacity.

Take the discharge process of Na||Na symmetric cell as an example, in the initial discharge process, nucleation overpotential exists because nucleation growth needs to overcome certain energy barriers, while the initial cycle of sodium nucleation process will be accompanied by the generation of SEI. The nucleation potential barrier will be more obvious, which is expressed as the gap between the discharge tip and the platform potential. At the end of the discharge in this cycle, a potential drop due to interfacial reorganization occurs. The voltage curve shows a spike in the potential drop. Thanks to the effective modulation of the SEI components by the PFDA-based electrolyte, the denseness of the SEI interior is increasing at the beginning of the cycle, which not only improves the Na$^+$ transport but also enhances the stability of the SEI, as shown by the overall improvement of ECDA for the overpotential in the charge-discharge curve and the substantial increase of the cycle life. However, as a dynamically changing

interfacial layer, the less stable and more soluble organic components in SEI cannot be eliminated, and there will be partial dissolution or electrochemical reactions. These small amounts of organic components (RONa, ROCO$_2$Na) will decompose into some inorganic substances (e.g., Li$_2$CO$_3$, Li$_2$O) after sodium stripping, forming a denser and more stable SEI layer. Therefore, the potential drop no longer occurs after cycling for a period, the growth overpotential gradually becomes larger than the nucleation overpotential, and the spikes become blunt or disappear. [13-16]

Table S6 Performance comparison and summary of Na||Na cells with different conditions and electrolytes in the reported research.

Electrolyte	Current density (mA cm^{-2})	Capacity (mAh cm^{-2})	Cycle Time	Journal
PFDA-based electrolyte	1	1	1700 h	This work
	2	4	350 h	
	5	1	100 h	
	1	10	1000 h	
1.0 M NaPF$_6$ in EC/PC/PhS$_2$Na$_2$-rich protection layer	1	1	800 h	*Angew. Chem. Int. Ed.* 2020, **16**, 6596.
	1	3	360 h	
	3	1	240 h	
1.0 M NaTFSI in FEC/EMC/Na$_3$P as protective layer	1	1	780 h	*Adv. Mater*. 2017, **29**, 1605512.
0.8 M NaPF$_6$ in TMP/FEC/5 wt% DTD	1	2	550 h	*Energy Stor. Mater.* 2021, **42**, 145.
	1	5	800 h	
	3	1	200 h	
1.0 M NaPF$_6$ in FEC/PC/HFE/5vol% PFMP	1	1	550 h	*Energy Environ. Sci.* 2020, **13**, 1788.
	1	5	800 h	
	5	1	200 h	
Na$_2$Te Protection layer with 1.0 M NaClO$_4$ in EC/DEC with5% FEC	1	1	700 h	*Energy Environ. Sci.* 2021, **10**, 382.
0.8 M NaPF$_6$ in FEC/EMC/HFE/SnF$_2$ Protection Layer	1	1	900 h	*Energy Environ. Sci.* 2021, **14**, 4936.
1.0 M NaPF$_6$ in TTE/FEC/DMTP	1	1	800 h	*Adv. Funct. Mater.* 2022, **26**, 2109378.
	5	1	150 h	
1.0 M NaPF$_6$ in EC/PC/2%TMTD	0.5	0.5	700 h	*Nano Lett.* 2021, **21**, 619.
	1	1	450 h	
1.0 M NaTFSI in TMP/FEC/HFE	1	1	800 h	*Adv. Funct. Mater.* 2021, **23**, 2103522.
	0.5	3	800 h	

2.0 M NaTFSI in TMP/FEC (7/3 by volume)	1	0.5	160 h	*Energy Stor. Mater.* 2019, **23**, 8.
	0.3	0.3	1000 h	
Na/MgF$_2$@RGO with 1.0 M NaClO$_4$ in EC/DEC/5% FEC	0.5	0.5	1600 h	*Adv. Energy Mater.* 2022, **12**, 2200990.
	1	1	500 h	
Na$_2$S/V/Na with 1.0 M NaClO$_4$ in EC/DEC/5% FEC	1	1	1000 h	*Adv. Mater.* 2022, **34**, 2109439.
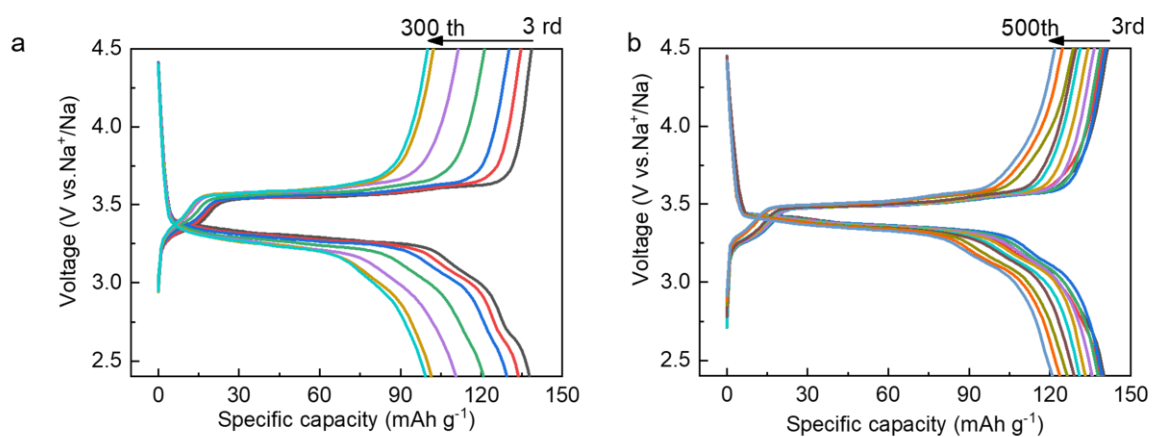
Fig. S41 Capacity-voltage curves of Na||PB full cells at different cycles with (a) PF-based electrolyte and (b) PFDA-based electrolyte at 1 C.
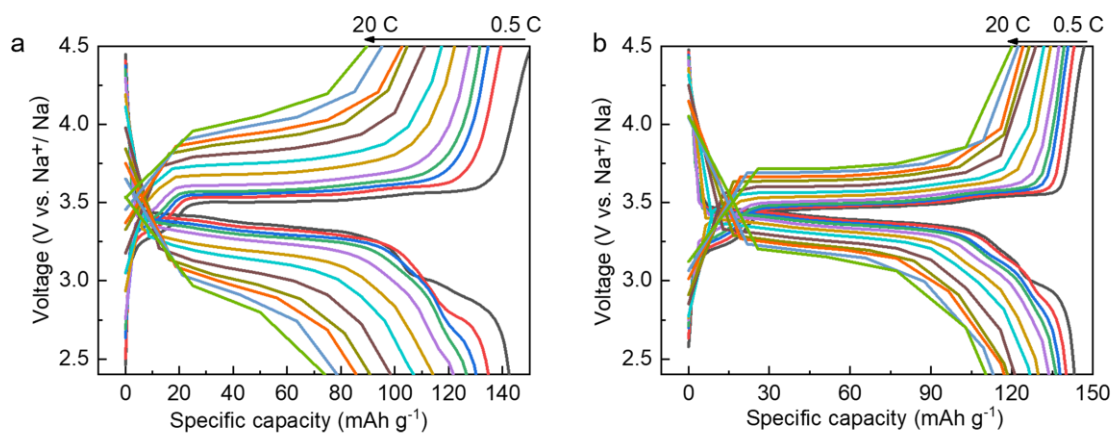
Fig. S42 Capacity-voltage curves of Na||PB cell with (a) PF-based electrolyte, (b) PFDA-based electrolyte at different rates.
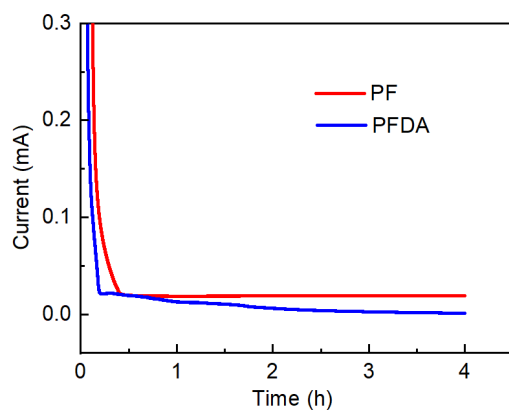
Fig. S43 Chronoamperometry (CA) curves of PB maintained at 4.5 V vs. Na⁺/Na with different electrolytes.
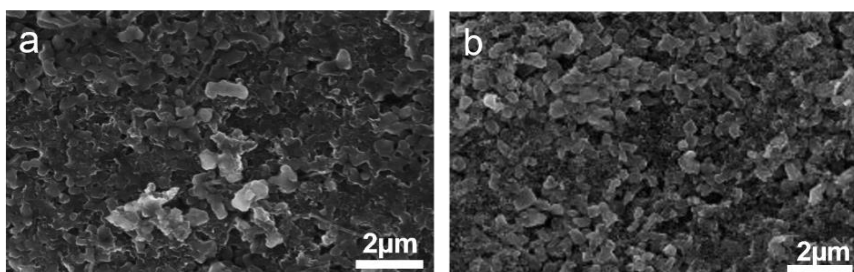
Fig. S44 Top-view SEM images of the PB cathode after 80 cycles in the (a) PF-based electrolyte, (b) PFDA-based electrolyte at 1 C.
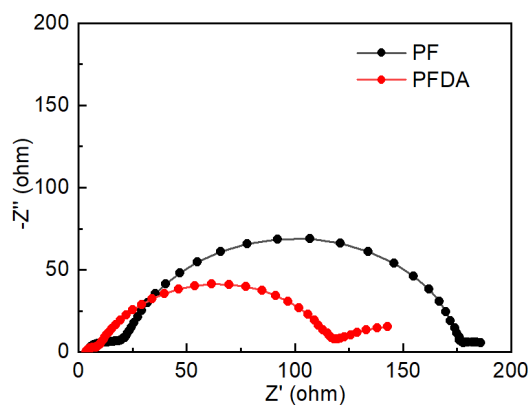
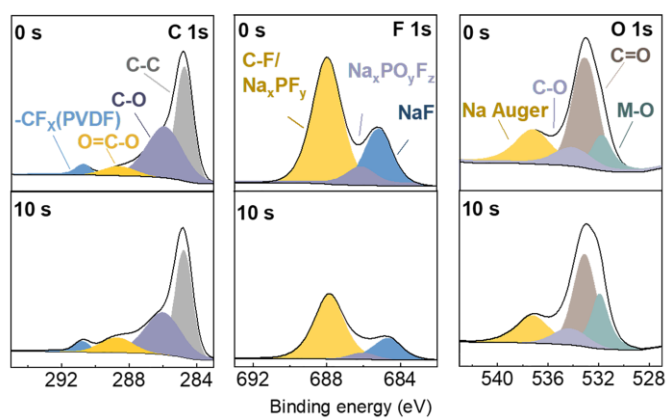Fig. S45 Nyquist plots of Na‖PB cells at 1 C in different electrolytes after 80 cycles.

Fig. S46 XPS spectra of the PB cathode in the PF-based electrolyte after 80 cycles.
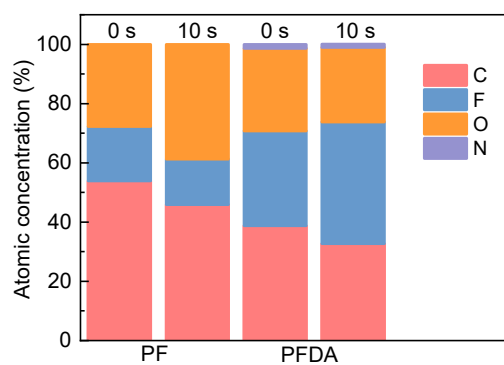
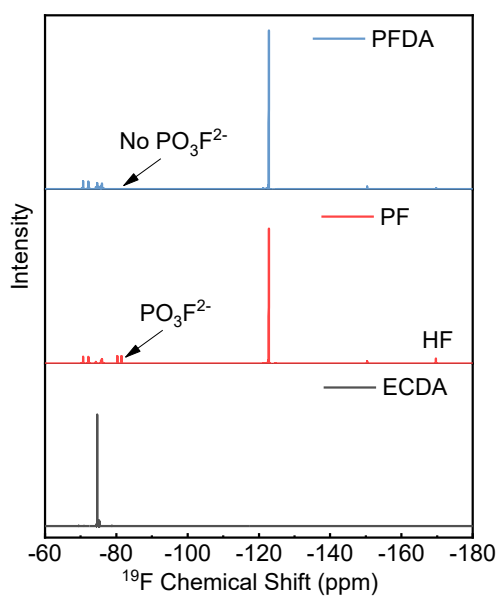Fig. S47 Atomic ratios of the C 1s, O 1s, N 1s and F 1 s of the PB cathode in different electrolytes.

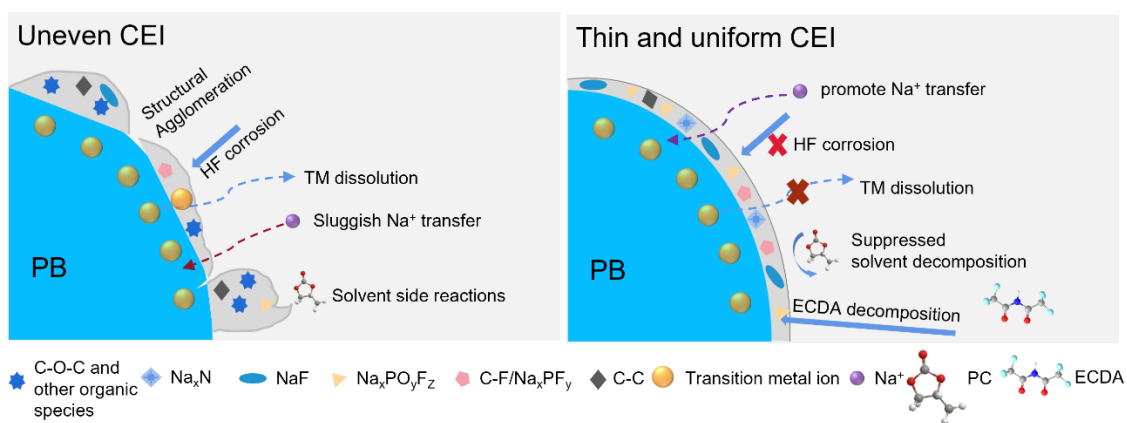Fig. S48 ^{19}F NMR spectra of the different electrolytes after adding 1000 ppm H_2O.

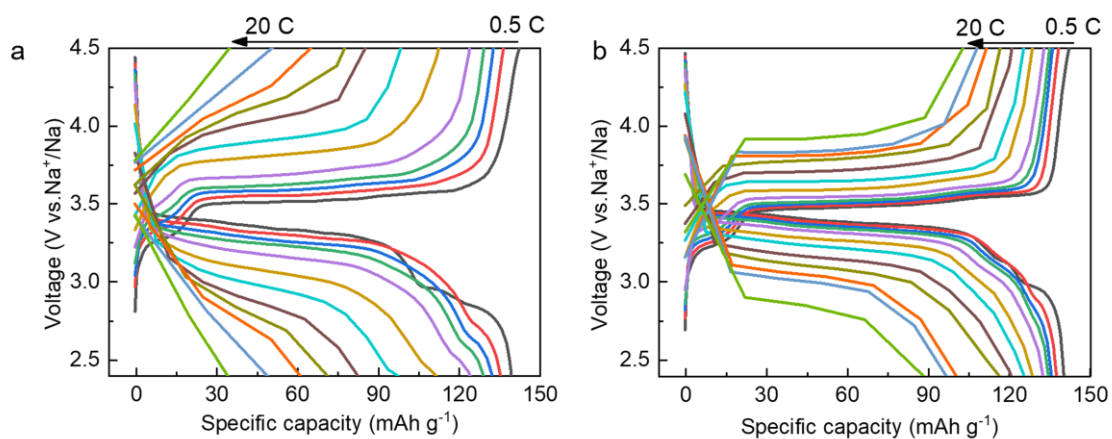Fig. S49 Schematic illustrations of the mechanism of PF-Based and PFDA-Based electrolytes induced CEI on PB.

Fig. S50 Capacity-voltage curves of Na||PB full cells with -10 °C in the (a) PF-based electrolyte, (b) PFDA-based electrolyte at different rates.
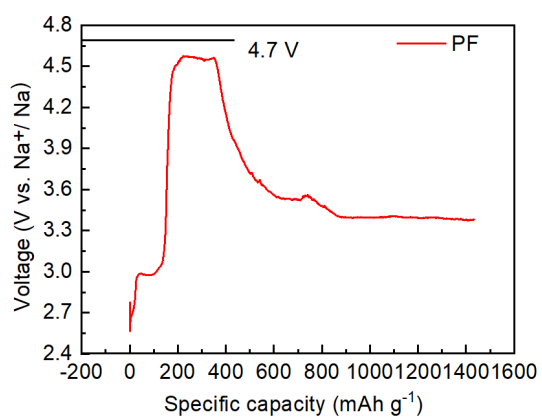

Fig. S51 Capacity-voltage curves of Na||PB full cells with a cut-off voltage of 4.7 V in the PF-based electrolyte.
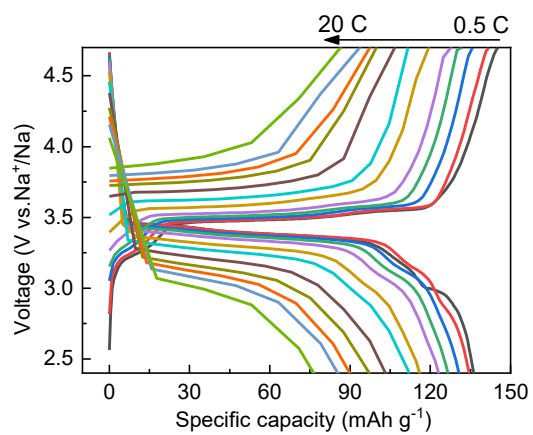
Fig. S52 Capacity-voltage curves of Na||PB full cells with a cut-off voltage of 4.7 V in the PFDA-based electrolyte in different rates.
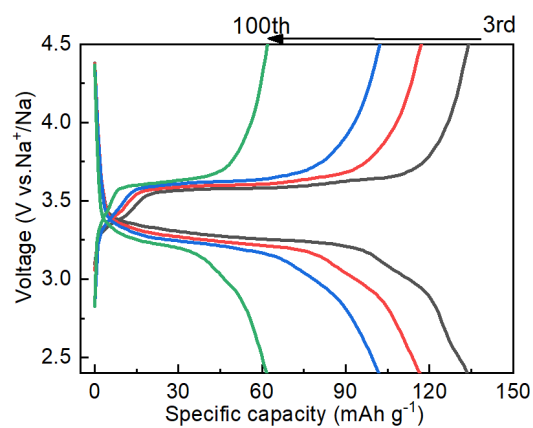

Fig. S53 Capacity-voltage curves of Na@Cu||PB full cells with a N/P ratio of 4:1 in the PF-based electrolyte at 1.5 C.
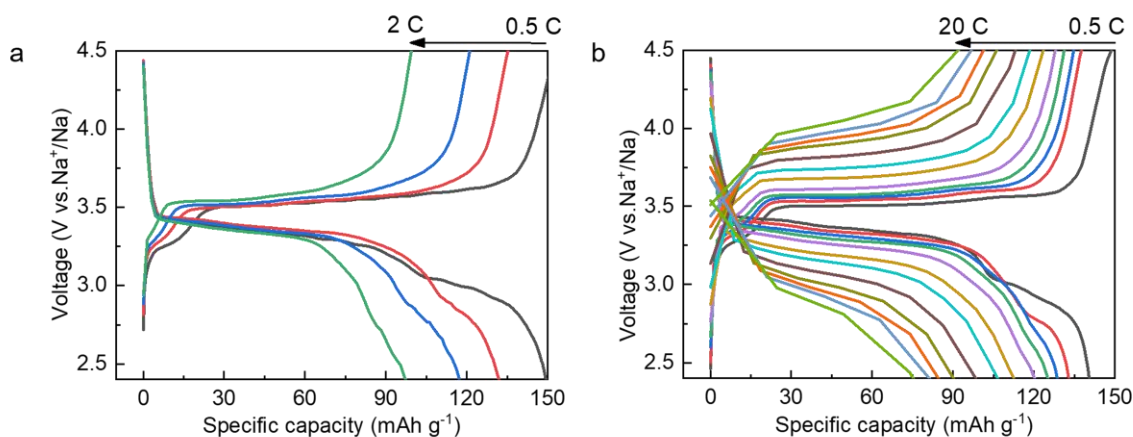
Fig. S54 Capacity-voltage curves of Na@Cu||PB full cells with a N/P ratio of 4:1 in the (a) PF-based electrolyte, (b) PFDA-based electrolyte at different rates.

References

1   M. N. Ovchinnikov, *Eur. Phys. J. Plus* 2017, **132**, 382.
2   B. G. Chae, S. Y. Park, J. H. Song, E. Lee and W. S. Jeon, *Nat. Commun.* 2021, **12**, 3814.
3   Z. Li, X. Huang, L. Kong, N. Qin, Z. Wang, L. Yin, Y. Li, Q. Gan, K. Liao, S. Gu, T. Zhang, H. Huang, L. Wang, G. Luo, X. Cheng and Z. Lu, *Energy Stor. Mater.* 2022, **45**, 40-47.
4   H. Su, Z. Chen, M. Li, P. Bai, Y. Li, X. Ji, Z. Liu, J. Sun, J. Ding, M. Yang, X. Yao, C. Mao and Y. Xu, *Adv. Mater.* 2023, e2301171.
5   R. Xu, J. F. Ding, X. X. Ma, C. Yan, Y. X. Yao and J. Q. Huang, *Adv. Mater.* 2021, **33**, e2105962.
6   L. Xiang, D. Jiang, Y. Gao, C. Zhang, X. Ren, L. Zhu, S. Gao and X. Zhan, *Adv. Funct. Mater.* 2023, 202301670.
7   F. A. Soto, P. Yan, M. H. Engelhard, A. Marzouk, C. Wang, G. Xu, Z. Chen, K. Amine, J. Liu, V. L. Sprenkle, F. El-Mellouhi, P. B. Balbuena and X. Li, *Adv. Mater.* 2017, **29**,18.
8   X. Ma, J. Yu, X. Zou, Y. Hu, M. Yang, F. Zhang and F. Yan, *Cell Rep. Phys. Sci.* 2023, **4**, 101379.
9   Y. Li and Y. Qi, *Energy Environ. Sci.* 2019, **12**, 1286.
10 Z. Tang, H. Wang, P. F. Wu, S. Y. Zhou, Y. C. Huang, R. Zhang, D. Sun, Y. Tang and H. Wang, *Angew. Chem. Int. Ed.* 2022, **61**, e202200475.
11 D. Li, Y. Sun, M. Li, X. Cheng, Y. Yao, F. Huang, S. Jiao, M. Gu, X. Rui, Z. Ali, C. Ma, Z. S. Wu and Y. Yu, *ACS Nano* 2022, **16**, 16966-16975.
12 Q. Zhao, S. Stalin and L. A. Archer, *Joule* 2021, **5**, 1119-1142.
13 S. Zhang, G. Yang, S. Liu, X. Li, X. Wang, Z. Wang and L. Chen, *Nano Energy* 2020, **70**, 104486.
14 Y. Jin, P. M. L. Le, P. Gao, Y. Xu, B. Xiao, M. H. Engelhard, X. Cao, T. D. Vo, J. Hu, L. Zhong, B. E. Matthews, R. Yi, C. Wang, X. Li, J. Liu and J.-G. Zhang, *Nat. Energy* 2022, **7**, 718-725.
15 L. A. Ma, A. J. Naylor, L. Nyholm and R. Younesi, *Angew. Chem. Int. Ed.* 2021, **60**, 4855-4863.
16 T. D. Pham, A. Bin Faheem, J. Kim, H. M. Oh and K. K. Lee, *Small*, 2022, **18**, 2107492.